# Hydrogen-Accelerated Fatigue of API X60 Pipeline Steel and Its Weld

Faucon, L.E.K.; Boot, T.; Riemslag, A.C.; Scott, S.P.; Liu, Ping; Popovich, V.

**DOI**
10.3390/met13030563

**Publication date**
2023

**Document Version**
Final published version

**Published in**
Metals

*metals*

MDPI

*Article*

# Hydrogen-Accelerated Fatigue of API X60 Pipeline Steel and Its Weld

**Lorenzo Etienne Faucon [1,*], Tim Boot [1], Ton Riemslag [1], Sean Paul Scott [1], Ping Liu [2] and Vera Popovich [1,*]**

[1] TU Delft Department of Materials Science & Engineering, Mekelweg 2, 2628 CD Delft, The Netherlands
[2] INTECSEA, Wilhelmina van Pruisenweg 2, 2595 AN Den Haag, The Netherlands
* Correspondence: l.faucon@hotmail.com (L.E.F.); v.popovich@tudelft.nl (V.P.)

**Abstract:** In this work, the hydrogen fatigue of pipeline steel X60, its girth welds and weld defects were investigated through in situ fatigue testing. A novel in situ gaseous hydrogen charging fatigue set-up was developed, which involves a sample geometry that mimics a small-scale pipeline with high internal hydrogen gas pressure. The effect of hydrogen was investigated by measuring the crack initiation and growth, using a direct current potential drop (DCPD) set-up, which probes the outer surface of the specimen. The base and weld metal specimens both experienced a reduction in fatigue life in the presence of hydrogen. For the base metal, the reduction in fatigue life manifested solely in the crack growth phase; hydrogen accelerated the crack growth by a factor of 4. The crack growth rate for the weld metal accelerated by a factor of 8. However, in contrast to the base metal, the weld metal also experienced a reduction of 57% in resistance to crack initiation. Macropores (>500 µm in size) on the notch surface reduced the fatigue life by a factor of 11. Varying the pressure from 70 barg to 150 barg of hydrogen caused no difference in the hydrogen fatigue behavior of the weld metal. The fracture path of the base and weld metal transitioned from transgranular and ductile in nature to a mixed-mode transgranular and intergranular quasi-cleavage fracture. Hydrogen accelerated the crack growth by decreasing the roughness- and plasticity-induced crack closure. The worst case scenario for pipelines was found in the case of weld defects. This work therefore highlights the necessity to re-evaluate pipelines for existing defects before they can be reused for hydrogen transport.

**Keywords:** hydrogen embrittlement; gaseous hydrogen fatigue; pipeline steel; weld defects; in situ mechanical testing; crack initiation; fractography



**Citation:** Faucon, L.E.; Boot, T.; Riemslag, T.; Scott, S.P.; Liu, P.; Popovich, V. Hydrogen-Accelerated Fatigue of API X60 Pipeline Steel and Its Weld. *Metals* **2023**, *13*, 563. https://doi.org/10.3390/met13030563

Received: 19 February 2023
Revised: 4 March 2023
Accepted: 8 March 2023
Published: 10 March 2023



## 1. Introduction

The ever-increasing concern about the impact of climate change on sectors important to society, such as human health and ecosystems, has prompted the necessity for a vast transition towards a sustainable society. As we are forced to adapt our methods of sourcing and utilizing energy, hydrogen has surged as a promising alternative energy source indispensable for climate neutrality [1]. Although the potential of hydrogen is well-known, its main distribution method, pipeline transportation, poses technical challenges in terms of reliability [2]. In particular, the possible introduction and diffusion of hydrogen into pipeline steel has garnered attention, as it can cause the reduction of ductility in metals, a phenomenon generally referred to as hydrogen embrittlement (HE). Another typical feature of HE is a reduction in fracture strength, thus the risk of pipeline rupture increases drastically. The interplay between the amount of (pressurized) hydrogen in the environment, the material's microstructure and the mechanical stresses govern the degree of HE [3]. Regarding the stresses, the hydrogen demand is known to fluctuate, which subjects the hydrogen-transporting pipelines to fatigue loading as a result of varying internal pressure.

A general consensus has been met on hydrogen increasing the growth rate of existing cracks under cyclic loading, which is referred to as hydrogen-accelerated fatigue crack growth (HA-FCG) [3–5]. The onset of the deleterious effect of hydrogen in the situation

of fatigue loading is associated with a stress intensity range of $\Delta K \approx 7–15$ MPa$\sqrt{m}$ [6–9]. This $\Delta K$ marks the beginning of HA-FCG, as generally observed from the transition to intergranular crack paths [7–10] and/or brittle quasi-cleavage fracture characteristics [11,12]. The onset of HA-FCG is commonly associated with a (sufficiently) steep hydrogen concentration at the crack tip region causing localized plasticity, which prevents crack tip blunting and promotes crack tip sharpening [6,13–15]. Pipeline welds, in particular, are considered to be at high risk of HE/HA-FCG failure due to: the combination of localized stress concentrations in weld misalignment, weld defects and the susceptible microstructure itself [5,16,17].

Several studies highlight that the moment until crack initiation governs the fatigue life in hydrogen environments [18–21]. The relative importance of crack initiation has been particularly emphasized in a study by Capelle et al. on X52 steels [22]. It was reported that the number of cycles until crack initiation in air was approximately 60% of the total fatigue life, whereas it was 80% under hydrogen influence. While such valuable information exists for base metals, a direct comparison to the initiation of hydrogen fatigue cracks in a weld metal is scarce in literature.

The results of Capelle et al. [22] were obtained using hydrogen electrolytic charging set-ups. Hydrogen diffusion in the steel is achieved in such set-ups by applying a constant potential or current that forces the reduction of $H^+$ ions to H atoms on the steel surface. In reality, however, hydrogen introduction into the pipeline steel is primarily influenced by exposure to the gaseous hydrogen environment. The associated mechanism for hydrogen entry into the steel is markedly different and the hydrogen equilibrium concentration in the subsurface layers of the steel is dependent on the partial pressure of the gaseous hydrogen [23–25].

Many studies looking into the possibility of transporting hydrogen in natural gas pipeline applications use (pre-)cracked specimens with sharp notches from which crack propagation occurs within the first few cycles [8,26–31]. The fatigue life is, however, mainly consumed by the initiation phase and the small-crack stage. Pre-cracking could therefore be considered a less accurate approach for the estimation of the overall fatigue life.

In this study, specimens were used with a blunt notch without pre-cracking, thereby capturing the behavior in the initiation phase and small crack stage as well. The crack initiation and growth were monitored through the direct current potential drop (DCPD) method, integrated in a novel in situ gaseous hydrogen charging fatigue set-up. The sample geometry mimics a small-scale pipeline with high internal hydrogen gas pressure, providing a close representation of industry practice. Base metal X60 steel and its girth weld were studied, including girth welds with actual weld pore defects from the fabrication process. This study thus allows a direct comparison between the base metal, weld metal, and weld-defected metal, and provides a critical assessment of their (hydrogen) fatigue performance by focusing on crack initiation.

## 2. Materials

The material examined in this research is API 5L X60 pipeline steel, which was extracted from a circumferential section of a subsea pipeline with a girth weld made from ESAB 70S-6 weldment steel. Even though the subsea pipeline was not used in industry, the girth weld conforms to industrial standards. The girth weld was made in accordance with the industry standard for pipe welding. The girth weld of the pipeline from which the specimens were extracted was made through automatic welding and is therefore viewed as being consistent along the circumference of the pipe. The macrostructure of the X60 girth weld is provided in Figure 1. The thickness of the pipe and weld are approximately 15.5 and 6.1 mm, respectively. The orientation of the material presented is indicated relative to the original X60 welded pipe: L—Longitudinal, C—Circumferential and R—Radial. The weld is classified as a butt weld that required multiple weld passes, directly observable from Figure 1. The first and last weld passes, as well as the start–stop locations of the welding process, were identified and excluded from the specimen geometry.

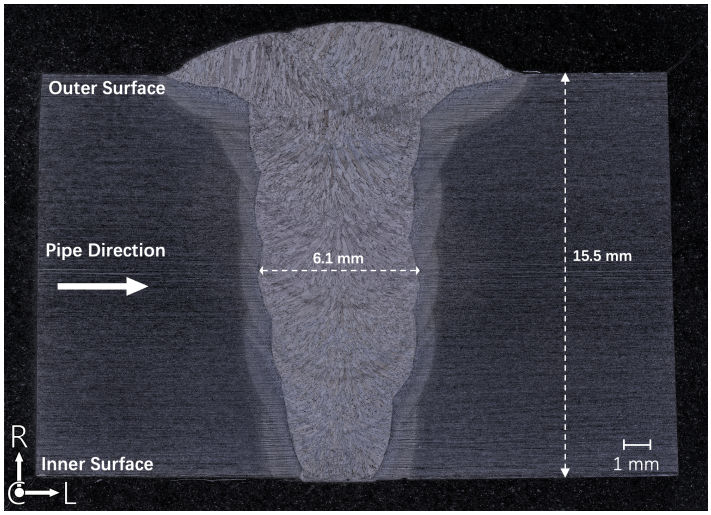


**Figure 1.** Macrostructure of the X60 girth weld. Relevant dimensions are annotated; the pipe-wall thickness is approximately 15.5 mm, the width of the weld is roughly 6.1 mm. The inner and outer surfaces are indicated, as well as the pipe direction. The orientation of the material in the pipe is indicated: L—Longitudinal, C—Circumferential and R—Radial. Etchant: nital (5%).

Figure 2 shows optical images of the microstructure of the base metal (BM) and weld metal (WM). As can be seen in Figure 2a, the BM is composed primarily of polygonal ferrite with a comparatively small proportion of pearlite. These microstructural phases of polygonal ferrite and pearlite can be characterized by their white and black appearance in the figure, respectively. From Figure 2b, it can be observed that the microstructure of the WM exhibits columnar coarse grains. Those grains represent prior austenite grains and can be identified from the characteristic appearance of the prior austenite grain boundaries (PAGBs).

Widmanstätten ferrite, which is visible as columnar lath-like structures, emanates from the prior austenite grain boundaries. Enclosed by the prior austenite grain boundaries are short ferrite needles that form the characteristic "basket weave pattern": a fine-grained interlocking microstructure called acicular ferrite. The grains differ significantly in size: approximately 5–10 µm for the polygonal ferrite in the BM and roughly 1 µm for the acicular ferrite in the WM. The width and length of the PAGBs are approximately 50 µm and 500 µm, respectively. The hardness of the BM and WM are $HV_1$ 199 ± 5 and $HV_1$ 239 ± 9, respectively. The alloy compositions of the base metal and weld metal are shown in Table 1 below. The data regarding this composition identification were extracted from work on the same pipeline material by Boot et al. [32]. In that particular study, composition analysis was performed using X-ray fluorescence scanning and LECO combustion analysis.

**Table 1.** X60 base metal and (girth) weld metal chemical composition. Bal represents Fe. The data are taken from [32].

| Element | C | Mn | Si | Cr | Nb | Al | P | S | Bal |
|---|---|---|---|---|---|---|---|---|---|
| Base Metal | 0.06 | 1.66 | 0.26 | 0.06 | 0.04 | 0.04 | <0.01 | <0.01 | 97.88 |
| Weld Metal | 0.07 | 1.45 | 0.58 | 0.05 | 0.01 | 0.01 | 0.01 | 0.01 | 97.81 |

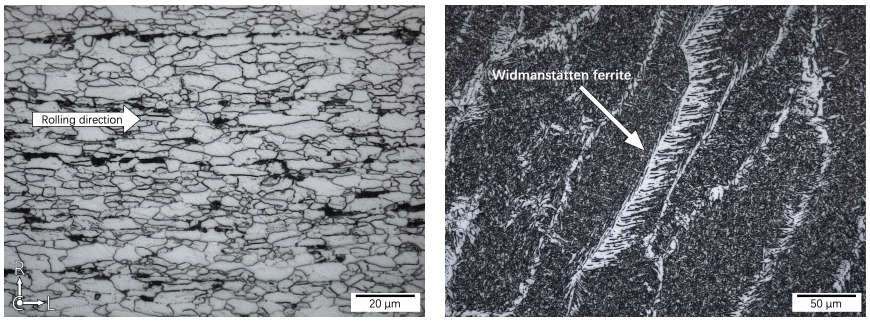


(**a**) (**b**)

**Figure 2.** (**a**) Microstructure of the base metal exhibiting polygonal ferrite (white) and colonies of pearlite (black) elongated extending along the rolling direction (white arrow). (**b**) Microstructure of the weld metal exhibiting fine-interlocking grains of acicular ferrite with Widmanstätten ferrite structures emanating from prior austenite grain boundaries. Etchant: nital (5%).

## 3. Methods

### *3.1. In Situ Gaseous Hydrogen Fatigue Set-Up Design*

The construction of the in situ gaseous hydrogen fatigue set-up is based on concurrent internal pressurization of a hollow specimen by hydrogen gas during fatigue tests. The set-up in this work was developed by modifying the in situ hydrogen gas slow strain rate tensile (SSRT) device engineered by Boot et al. into one compatible with in situ fatigue testing [32]. The main difference regarding the set-up is that in this study, a hydraulic 4-column load frame (MTS 311.21 ServoHydraulic 350 kN Load Frame) is used, integrated with flexible (clevis to clevis) self-aligning adapters. In addition, components for the DCPD method were produced, which will be addressed separately in the associated section (Section 3.2).

Hollow cylindrical specimens were machined from the longitudinal direction of an X60 pipe section, as illustrated in Figure 3a. In Figure 3b, a zoomed-in normal projection of the pipe wall is given, where the two specimens in Figure 3a are identified as a WM and BM sample. The specimen geometry is shown in Figure 3c and includes an internal circumferential notch semi-circular in shape with a radius and depth of 0.75 mm. This notch design induces a stress concentration factor ($K_t$) of ≈3.0, allows control of the location of failure, and reflects a failure that is more representative of reality: cracks that initiate on the inside of the pipe and develop outward until failure. In addition, the notch represents imperfections inherently existing in pipelines, either from fabrication, handling, transport, installation, or operation (i.e., by 3rd party impact). The notch was machined using the die sink electrical discharge machining technique and is located in the center of the girth weld. The WM specimens can thus be considered as a small scale pipe that includes a matching girth weld. The internal surface, and thus also the notch, of the specimens were polished to a 1000 grit finish. The specimens were then ultrasonically cleaned with 2-isopropanol for 5 min.

As can be seen from Figure 3c, the specimen design contains a step at one of its ends. A nitrile O-ring is placed in this designed step to create a sealed connection between the specimen and adapter after mounting through the M14x2 threads. The other end of the specimen is closed airtightly by placing an annealed copper washer under an M6x1 bolt head which, by tightening the bolt into the internal threads of the specimen, seals the hole. An enclosed volume is now created that extends from the hydrogen supply piping to the sample itself. Through this approach, the specimen is internally pressurized.

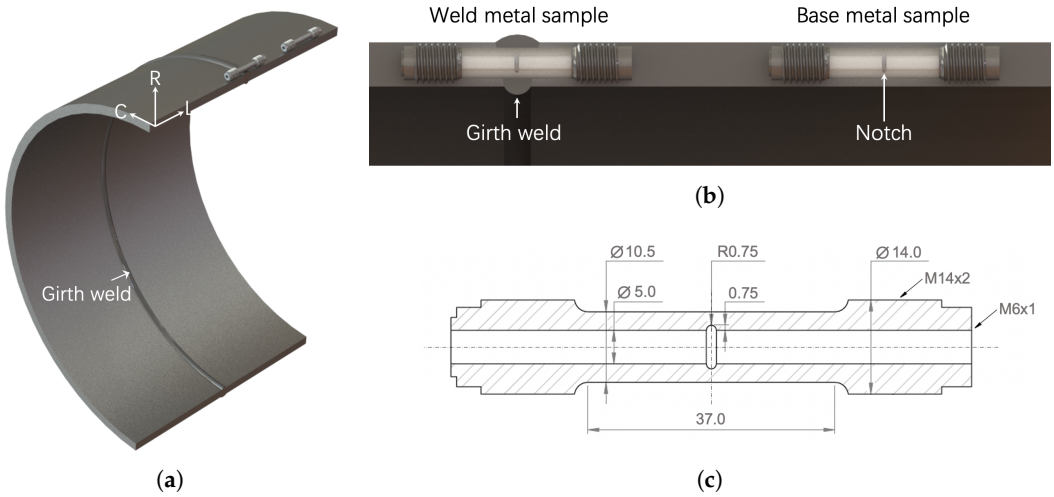


**Figure 3.** (**a**) Illustration of a cross-section of an X60 pipe including the girth weld and two samples, from which the orientations of the prepared samples can be derived: L—Longitudinal, C—Circumferential and R—Radial. (**b**) The zoomed-in normal projection of the pipe wall, which identifies the two samples as a weld metal and base metal sample. The transparent view of the gauge allows the orientation of the notch in the material to be seen. (**c**) Engineering drawing showing the geometry of the specimen and notch. Dimensions are in mm.

### *3.2. Direct Current Potential Drop*

DCPD was used to measure crack initiation and growth throughout the experiments. The DCPD technique relies on the flow of a current through the specimen. A copper strip to which the DCPD's current cables were connected via a bolted connection was firmly fastened around both adapters to feed the current from the DCPD apparatus to the specimen. M2 bolts were utilized as DCPD probes that measured the voltage on the external surface of the specimen. The probes were held in place by a 3D-printed tubular structure of polylactic acid (PLA), referred to as the "probe holder", which surrounded the gauge of the specimen. Brass heat inserts were anchored into the probe holder, since their internal threads allowed for fixation of the probing locations. Figure 4a provides an illustration of a cross-sectional view of a specimen and the placement of the probe holders including the heat inserts and probes. The voltage deflection due to crack initiation and growth, $\Delta V$, was measured by the probes distanced 1.75 mm from either side of the semi-circular notch.

The other bolts were spaced 14.0 mm from the edge of the notch. Their voltage deflection output, $\Delta V_0$, was not influenced by changes in crack size. Those probes are therefore the reference probes and accounted for environmental changes influencing the measured voltages.

Figure 4b illustrates a top view of the cross section of the specimen and probe holder. At each of the bolts' heights shown in Figure 4a, three bolts are placed equidistantly along the circumference of the gauge. These three bolts were installed into a parallel circuit connection.

For proper crack measurements, the specimen is required to be electrically insulated from its conductive mechanical connections. Appropriate measures were taken to insulate the specimen: (i) dielectric fittings (SS-4-DE-6 Swagelok) were inserted between the connections of the adapter with the gas transportation piping system, and (ii) glass fiber plates were placed between the wedge grips and hydraulic grips of the fatigue testing machine.

The output of the DCPD device is the potential drop, $\frac{\Delta V}{\Delta V_0}$, as a function of time. To calibrate the DCPD, fatigue tests were stopped prematurely and a brittle fracture was induced using liquid nitrogen. The fatigue surface area could then be measured with a digital microscope (Keyence VHX-5000) and correlated to the potential drop. The crack initiation point is identified as a threshold of a 150% increase in the slope relative to the baseline voltage slope, which corresponds to a crack surface area of $\approx$0.6 mm$^2$.

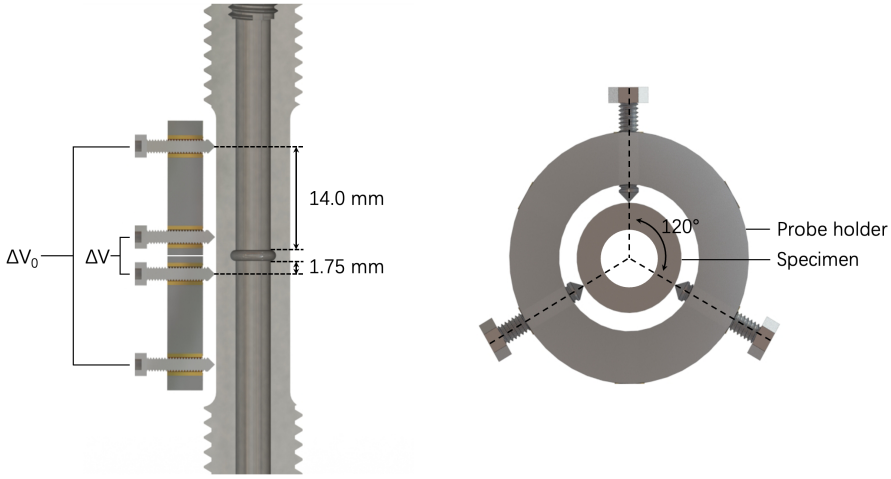


(**a**) (**b**)

**Figure 4.** Illustration of the positions of the DCPD probes. (**a**) Cross-sectional view of the specimen and two stacked probe holders. The brass elements represent the internally threaded heat inserts. $\Delta V_0$ and $\Delta V$ indicate the potential drop measurement locations of the reference probes over the gauge and the probes over the notch, respectively. The distance between the measurement location of these probes and the side of the notch are annotated. (**b**) Top cross-sectional view of the gauge of the specimen and the probe holder. The three probes are equidistantly arranged along the circumference.

### *3.3. Test Settings and Procedures*

The fatigue tests were force-controlled and performed with the following fatigue test conditions: frequency ($f$) of 8 Hz, load ratio ($R$) of 0.1, $F_{min}$ of 1.71 kN ($\sigma_{nom,min}$ = 25.6 MPa) and $F_{max}$ of 17.1 kN ($\sigma_{nom,max}$ = 256.0 MPa). Note that the nominal stress, $\sigma_{nom}$, refers to the stress experienced in the gauge section. Even though on- and offshore operating pipelines typically experience pressure fluctuations of $\leq$1 Hz, this study performs hydrogen fatigue tests at 8 Hz. This decision prevented overnight testing, for which the research facility could not accommodate due to safety reasons. As discussed in a study by Nanninga et al., no significant differences in the hydrogen-assisted fatigue crack growth rate (HA-FCGR) are observed between tests performed within a range of 0.1–10 Hz [3]. Therefore, 8 Hz is considered sufficiently applicable, while being economical in terms of test duration.

A current of 20 A was applied for the DCPD experiments and a pulse divider was used, which ensured that the applied current was pulsed four times within one loading cycle of the load cell to reduce any self-heating effects. The DCDP signal is triggered at the moment of the maximum fatigue load, to minimize the effect of crack closure on the voltage output. The end-of-test criterion was defined as fracture itself, indicated by the moment when the load drops 5% below the minimal force of the fatigue cycles.

The specimens tested in an $H_2$ environment were pre-charged for at least 7 h to allow $H_2$ to diffuse into the specimen and to reach an equilibrium diffusion state within the steel. Prior to pre-charging, the piping system was flushed with $N_2$ and evacuated thrice to exclude any oxygen contamination in the pressurized gas to which the specimen is subjected. After the final evacuating step, the system (with specimen) was filled with $H_2$ gas and pressurized to the test pressure. After the pre-charging period, the fatigue test started under this held pressure. When the $H_2$ fatigue tests were finished, the system was flushed with $N_2$ in order to evacuate any residual $H_2$ gas in the set-up.

#### Test Matrix

Three groups of specimens were fatigue tested in this research: notched BM X60, notched girth WM and notched girth WM with weld defects. The weld defects were identified post-mortem as macropores with an approximate length or width greater than

500 µm resulting from the welding procedure. A more detailed overview of the defect sizes and locations in the material can be read in Section 4.4.1.

The BM specimens were tested in ambient conditions to obtain information on the basic fatigue performance of the X60 steel with the specimen geometry. Both the BM and non-defective WM samples were tested under 150 barg $N_2$ and 150 barg $H_2$ to study the effect of high pressure gas and hydrogen gas on the crack initiation and growth of fatigue cracks. The non-defective WM samples included additional tests at 70 barg $H_2$ gas in order to determine the influence of the pressure level. The defected WM samples only comprise data of tests performed at 150 barg $H_2$ gas. An overview of these test conditions is provided in Table 2. Each combination of specimen type and environment contains crack initiation and growth data from at least three experiments.

**Table 2.** Summary of the different subgroups of tested notched base metal (BM) and weld metal (WM) specimens. The specimen group "Notched WM Defected" refers to WM specimens with macropores (>500 µm in size).

| Gas | Notched BM | Notched WM | Notched WM Defected |
|---|---|---|---|
| Air | 0 barg | Not tested | Not tested |
| $N_2$ | 150 barg | 150 barg | Not tested |
| $H_2$ | 150 barg | 70, 150 barg | 150 barg |

For each subgroup of specimens, the number of cycles until crack initiation ($N_I$) and number of cycles until failure ($N_F$) were measured. The fatigue life of the specimens was distinguished based on their crack initiation phase, represented by $N_I$, and the growth phase ($N_G = N_F - N_I$). The data are further represented as the percentage of lifetime spent in the crack initiation phase ($L_I$):

$$L_I = \frac{N_I}{N_F} \times 100\% \quad (1)$$

Scanning electron microscopy (SEM) fractography with a JEOL JSM IT-100 machine was performed on post-mortem specimens to identify fracture morphologies characteristic of hydrogen-accelerated fatigue. Crack path analysis was conducted by aborting the fatigue tests at a 3.0–4.0% increase from the baseline potential drop voltage, as this value was known to correspond to a distinct crack length. The samples were then embedded in resin, thinned using a lathe, polished and etched to observe the crack trajectory and its dependency on the microstructure in a Leica Microsystems Wetzlar GmbH light microscope. In addition, for the crack path analysis, Electron Backscatter Diffraction (EBSD) data were acquired on a Thermo Fisher HeliosTM UXe G4 PFIB scanning electron microscope. An accelerating voltage of 20 kV, a current of 3.2 nA, and a step size of 0.05 micron were used. Team™ and EDAXTSL-OIM Analysis™ software were used for post-processing.

## 4. Results and Discussion

### *4.1. Hydrogen-Accelerated Fatigue of the Base Metal*

Figure 5 below shows the fatigue results of the BM in a bar graph. The data used to plot the graph is summarized in Table 3. It can be inferred that the change in environmental conditions did not significantly affect the crack initiation period ($N_I$) for the BM; the averages and standard deviations of $N_I$ are effectively within the same range. The absence of the influence of $H_2$ on $N_I$ agrees with the work of Arnaudov [33]. According to Arnaudov, hydrogen has no influence on crack initiation when tested at a total strain amplitude of $\leq$0.20%. According to various researchers, a sufficiently high cyclic strain causes hydrogen-induced slip localization, which in turn lowers $N_I$ [33–36]. The findings presented in this work are in line with this statement since fatigue was in the elastic range. Although no

significant change in $N_I$ was observed, the presence of 150 barg $H_2$ did reduce the $N_F$ by accelerating the growth phase.

The data can be further inspected by normalizing the results to the ones of 150 barg $N_2$. The normalized $N_F$ of 150 barg $H_2$ is 63%, when presented as a percentage. The presence of hydrogen thus decreased the lifetime by 100% − 63% = 37%. The normalized $N_G$ in $H_2$ reduced to 24.8% of that in $N_2$, indicating that the detrimental effect of $H_2$ on the fatigue lifetime manifested by accelerating the overall crack growth by a factor of 4.

The $L_I$ of air, 150 barg $N_2$ and 150 barg $H_2$ are 54.2 ± 3.1%, 58.5 ± 3.4%, and 83.6 ± 0.5%, in respective order. Those values are in line with the ones of Capelle et al. [22], who reported an $L_I$ of ≈60% and 80% for air and $H_2$, respectively. Capelle et al. used a hydrogen electrolytic charging test set-up and roman tile specimens. Thus, although in this work the charging method and sample geometry are different, no notable difference in the fraction of lifetime spent until crack initiation is observed. This is unexpected, as it has been reported that different charging techniques lead to significant differences in the amount of hydrogen and its distribution in steel [25].

The slight difference in $N_G$ of air ($93.6 \times 10^3$) and 150 barg $N_2$ ($84.0 \times 10^3$) is attributed to the gas pressure increasing the triaxial stress state at the crack tip, thereby accelerating the crack growth rate. The $L_I$ in 150 barg $H_2$ (83.6%) is distinctly higher compared to the other environments. Crack initiation, rather than growth, thus governs the fatigue life in the $H_2$ environment. This finding is in agreement with the trend in the literature [18–22].

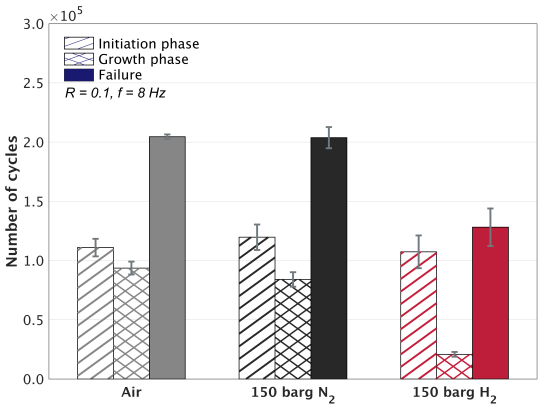


**Figure 5.** Bar graph of the number of cycles spent in the crack initiation phase ($N_I$) and the growth phase ($N_G$), and the total number of cycles until failure ($N_F$) of the base metal specimens. The different environments tested are shown with distinct colors. The single and double hatched bars represent the number of cycles spent in the initiation and growth phase, respectively. Error bars are standard deviations.

**Table 3.** An overview of the base metal fatigue results, presenting the number of cycles spent in the crack initiation phase ($N_I$), the growth phase ($N_G$), the cycles until failure ($N_F$) and percentage of lifetime spent in the crack initiation phase ($L_I$). Errors are standard deviation.

| Environment | $N_I$ [×10³] | $N_G$ [×10³] | $N_F$ [×10³] | $L_I$ [%] |
|---|---|---|---|---|
| 0 barg Air | 110.9 ± 7.4 | 93.6 ± 5.4 | 204.6 ± 2.0 | 54.2 ± 3.1 |
| 150 barg $N_2$ | 119.7 ± 10.8 | 84.0 ± 6.1 | 203.7 ± 8.9 | 58.5 ± 3.4 |
| 150 barg $H_2$ | 107.3 ± 13.9 | 20.8 ± 2.0 | 128.2 ± 15.9 | 83.6 ± 0.5 |

### *4.2. Hydrogen-Accelerated Fatigue of the Weld Metal*

Figure 6 presents the fatigue results of the WM in a bar graph. The data used to plot the graph, along with the BM fatigue data in pressurized environments, are summarized in Table 4. The WM has a superior fatigue resistance compared to the BM under the concerned test conditions. Namely, the $N_F$ of WM in 150 barg $N_2$ is a factor of 2.1 higher than that of

the BM in the similar environment. Translating this into the concept of fatigue resistance, it can be calculated that the WM lifetime increased by ≈113%. This result is inherent to the microstructure. The finer grains in the WM generally give the material higher strength and toughness, thereby increasing its resistance to fatigue. Note that the difference in strength between the BM and WM can be readily inferred from the marked difference in hardness observed in Section 2.

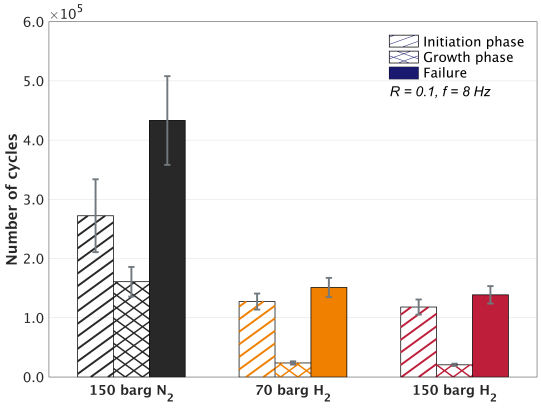


**Figure 6.** Bar graph of the number of cycles spent in the crack initiation phase ($N_I$) and the growth phase ($N_G$), and the total number of cycles until failure ($N_F$) of the weld metal specimens. The different environments tested are shown with distinct colors. The single and double hatched bars represent the number of cycles spent in the initiation and growth phase, respectively. Error bars are standard deviations.

**Table 4.** An overview of the pressurized base and weld metal fatigue results presenting the number of cycles spent in the crack initiation phase ($N_I$), the growth phase ($N_G$), the cycles until failure ($N_F$) and percentage of lifetime spent in the crack initiation phase ($L_I$). Errors are standard deviation.

| Material | Environment | $N_I$ [$\times 10^3$] | $N_G$ [$\times 10^3$] | $N_F$ [$\times 10^3$] | $L_I$ [%] |
|---|---|---|---|---|---|
| Base metal | 150 barg $N_2$ | 119.7 ± 10.8 | 84.0 ± 6.1 | 203.7 ± 8.9 | 58.5 ± 3.4 |
| | 150 barg $H_2$ | 107.3 ± 13.9 | 20.8 ± 2.0 | 128.2 ± 15.9 | 83.6 ± 0.5 |
| Weld metal | 150 barg $N_2$ | 272.3 ± 61.5 | 160.8 ± 25.1 | 433.1 ± 75.0 | 61.3 ± 4.8 |
| | 70 barg $H_2$ | 127.4 ± 13.5 | 23.7 ± 2.7 | 151.1 ± 16.3 | 84.3 ± 0.1 |
| | 150 barg $H_2$ | 118.2 ± 12.8 | 20.6 ± 2.0 | 138.8 ± 14.7 | 85.1 ± 0.3 |

The salient feature of Figure 6 is that the hydrogen has a deleterious effect on the WM fatigue life by affecting both $N_I$ and $N_G$. This is in contrast to BM, where the $N_I$ was not affected. Therefore, in the WM, $H_2$ reduces the resistance to crack initiation and accelerates the fatigue crack growth rate. Regarding the 150 barg $H_2$ environment, the average number of cycles until failure is a factor of 3.1 smaller compared to the 150 barg $N_2$ environment. Varying the $H_2$ gas pressure from 150 barg to 70 barg does not influence the fatigue life, $N_F$; the results fall within the same range.

The phenomenon that the hydrogen fatigue behavior of the WM is independent of the gas pressure contradicts the assertion of Holbrook et al. that the dependence of the fatigue crack growth rate (FCGR) on hydrogen pressure is of the power 0.36 [37]. In such a case, an almost $(\frac{150\text{ barg}}{70\text{ barg}})^{0.36} = 1.32$ times faster crack growth rate would have been present. A noticeably higher $L_I$ would then have to be exhibited by the 150 barg $H_2$ environment. The contradictory finding could be a result of more recently discovered phenomena such as a maximum hydrogen saturation in the cracking process zone being reached [38], or that a critical hydrogen concentration was reached [6]. Researchers have emphasized that a critical ΔK must be reached to neglect the gas pressure dependence of the HA-FCGR [6,39].

The data in this work virtually covers a range of ΔK starting at zero and, if it were to exist, such an onset must therefore be observed. It could be that the HA-FCGR before the critical ΔK was so subtle that the effect on $N_I$ and $N_F$ was within the standard deviation range of the 150 barg and 70 barg $H_2$ tests. In this case, the HA-FCGR difference before the pressure independence onset did not affect the total fatigue behavior nor life.

Regarding the percentage of lifetime spent in the crack initiation and growth phase, the BM and WM behave relatively similarly: BM 150 barg $H_2$ $L_I \approx 84\%$ versus WM 150 barg $H_2$ $L_I \approx 85\%$, and BM 150 barg $N_2$ $L_I \approx 59\%$ versus WM 150 barg $N_2$ $L_I \approx 61\%$. This indicates that the change of environment does not affect the two materials differently regarding the relative reduction of the initiation and growth phases.

By comparing the normalized $N_F$ of the WM and BM, it can be observed that the effect of hydrogen is more deleterious for the WM. The presence of 150 barg $H_2$ reduced the resistance to crack initiation by 57%. For the WM, the growth phase accelerated by a factor of 8, which is 4 for the BM. Ultimately, for the WM, the total reduction in fatigue life due to hydrogen is 68%, whereas this is 37% for the BM. Thus, the effect of hydrogen on the reduction in lifetime is a factor of 1.8 higher for the WM.

### *4.3. Fractography*

#### 4.3.1. Base Metal Fractography

Figure 7a,b provide a sectional macroscopic overview of BM fractured surfaces tested in 150 barg $N_2$ and $H_2$, respectively. The air environment is excluded for further discussion in this work, since the fracture behavior is macro- and microscopically similar to 150 barg $N_2$. Figures 7a,b view a section of the wall ligament of the specimen. The top side of the fracture surface relates to the inner surface and a section of the notch. The bottom side corresponds to the external surface of the specimen. The internal circumferential notch enforced fracture at the notch root. Cracks initiated at multiple origins and propagated on different planes. These propagating fatigue cracks intersected through steps between neighboring planes, thereby creating ratchet marks, which are indicated with black arrows in the figure. The formation of these characteristic ratchet marks is indicative of a sharp stress concentration created by the designed notch [40]. The ratchet marks are macroscopically visible as lines parallel to the overall crack growth direction, which is annotated in the figure.

The fracture surface in 150 barg $N_2$ is completely ductile and transgranular in nature, whereas in hydrogen the fatigue region exhibits two different appearances: (i) ductile and transgranular fracture, and (ii) brittle quasi-cleavage fracture. Figure 7c shows a close-up view of the notch of a 150 barg $H_2$ tested sample. It can be inferred that the initial crack growth in hydrogen is ductile, similar to that in nitrogen. The absence of embrittlement effects in this early stage of fatigue elucidates the finding from the mechanical tests that hydrogen did not affect the crack initiation moment in the BM.

Figure 7d is a higher magnification image of section I enclosed by the red rectangle in Figure 7b. This image provides an overview of the transition in fracture behavior in hydrogen, which marks the onset of HA-FCG. The onset of HA-FCG has previously been associated with a $\Delta K \approx 7$–$15\ \mathrm{MPa}\sqrt{\mathrm{m}}$ [12,41]. The critical ΔK for HA-FCG in this study is estimated to be starting from $15\ \mathrm{MPa}\sqrt{\mathrm{m}}$, which agrees well with the literature. It is important to note that this is a rough approximation, as a formula for ΔK for this specific (novel) geometry has not yet been formulated.

The fracture surface at the onset of HA-FCG is often characterized to be predominantly intergranular [30,41,42]. In this work however, the onset of HA-FCG is primarily transgranular, but exists as a mixed-mode of intergranular features. The intergranular features are identified by the triple points (red arrows) on the fracture surface. The other arrows (blue) indicate the locations of secondary cracking in the material. As the crack front progressed, the prevalence of secondary cracking increased. This is visible in Figure 7e, which provides a close-up view of section II in Figure 7b. The brittle quasi-cleavage fracture behavior is clearly visible; the characteristic smooth features on an irregularly faceted fracture surface are annotated with yellow arrows.

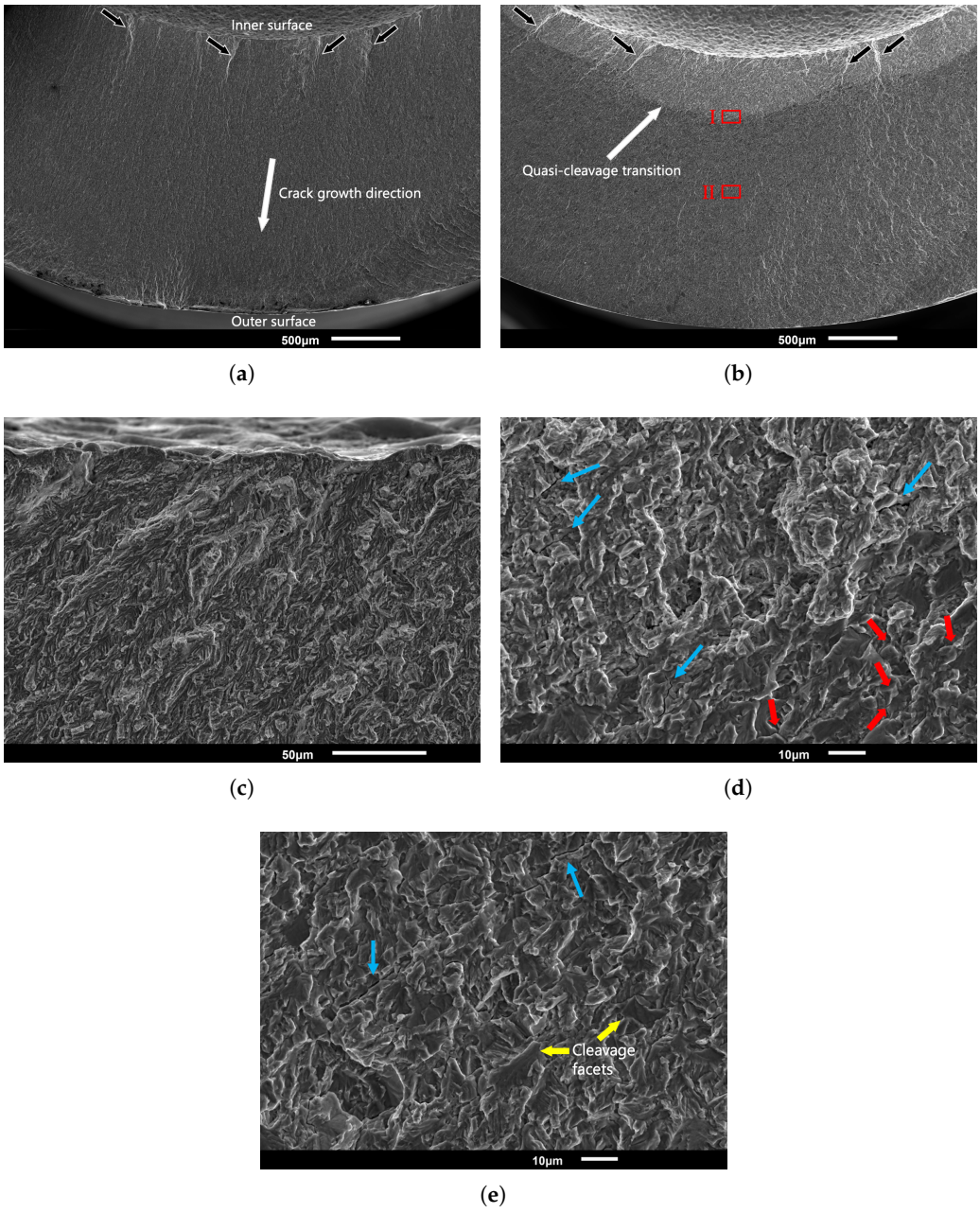


**Figure 7.** SEM fractographic images of notched base metal samples. (**a**) Macroscopic overview of a 150 barg $N_2$ and (**b**) a 150 barg $H_2$ tested sample. The black arrows indicate ratchet marks. (**c**) Zoomed-in view of the notch of a 150 barg $H_2$ tested sample. (**d**) Higher magnification view of Area I in (**b**) showing the quasi-cleavage transition. (**e**) Higher magnification view of Area II in (**b**) in which cleavage facets are clearly visible. The blue and red arrows indicate secondary cracking and triple points, respectively.

#### 4.3.2. Weld Metal Fractography

Figure 8a,b provide a sectional macroscopic overview of WM fractured surfaces tested in 150 barg $N_2$ and $H_2$, respectively. The fractographic images of 70 barg $H_2$ are excluded from this section since they are nearly identical to the ones of 150 barg $H_2$, which is expected based on the similar fatigue behavior observed in Section 4.2.

Cracks initiated at the inner surface of the notch, similar to the BM samples. The associated ratchet marks are illustrated with black arrows. In the presence of hydrogen, the fracture surface exhibits large brittle cleavage facets (see yellow arrows). These cleavage

facets are relatively consistent in orientation and appearance, and are associated with fracture along the prior austenite grain boundaries.

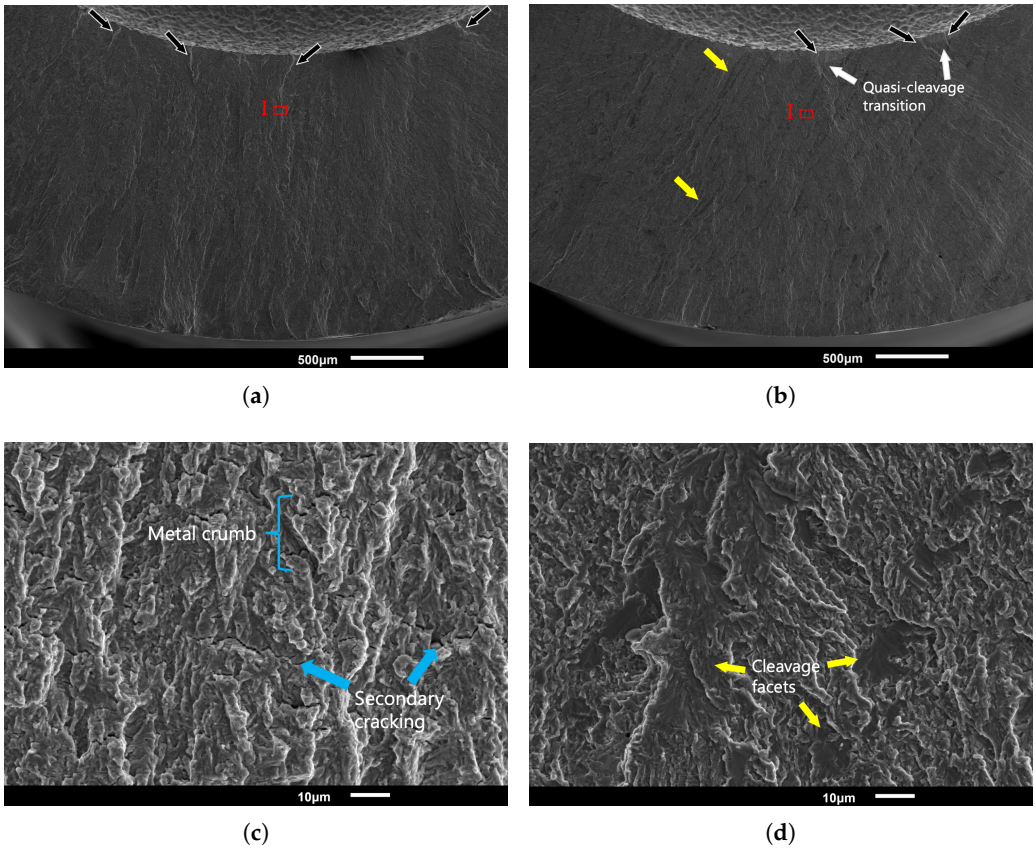


**Figure 8.** SEM fractographic images of notched weld metal samples. (**a**) Macroscopic overview of a 150 barg $N_2$ and (**b**) a 150 barg $H_2$ tested sample. The black arrows and yellow arrows indicate ratchet marks and quasi-cleavage facets along prior austenite grain boundaries, respectively. (**c**) Zoomed-in view of Area I in (**a**) showing metal crumbs and secondary cracking. (**d**) Zoomed-in view of Area I in (**b**) showing quasi-cleavage facets and intergranular fracture.

Unlike the BM, the HA-FCG transition for the WM is not well-defined and it appears that the embrittlement effect of hydrogen manifests primarily from the instant of crack initiation. The fact that pressurized hydrogen affected the $N_I$ of the WM, and not that of the BM, is directly related to the microstructure. The WM contains finer ferrite grains, which means that the grain boundary area in the material is larger compared to that of the BM. In a study conducted by Marsh and Gerberich, it was concluded that hydrogen fatigue crack initiation is intensified at grain boundaries located at the specimen surface [43]. Thus, in terms of grain boundary density at the surface of the notch, there is a higher probability of cracking at the grain boundaries for the WM. Furthermore, after crack initiation, the increased density of grain boundaries efficiently traps a high volume fraction of hydrogen, thereby also promoting crack growth.

Figures 8c,d present a zoomed-in view of Area I annotated in Figure 8a (150 barg $N_2$) and 8b (150 barg $H_2$), respectively. The main difference between the $N_2$ and $H_2$ samples is that secondary cracking is absent for $H_2$. Examples of secondary cracking in $N_2$ are illustrated with blue arrows in Figure 8c. In addition, a metal crumb is identified that appears as a rough fragment protruding from the surface on the fracture. In order to shed light on the crack tortuosity, Figure 9a is inspected, which presents the crack path in 150 barg $N_2$. It can be seen that the rejoining of the branched cracks results in the metal crumb formation [44,45]. The extent of this metal crumb formation and secondary

cracking clearly indicate that the crack trajectory in $N_2$ exhibits a high degree of tortousity. There exists a general tendency that high tortuosity of a crack path can provide enhanced fatigue performance [44,46]. Higher fatigue performance is related to crack tip stress-shielding induced by crack deflection and branching. In addition, the uneven crack surfaces associated with high crack tortuosity do not match perfectly during unloading, thereby reducing the effective stress intensity at the crack tip. The lower FCGR in $N_2$ thus resulted from the phenomena of plasticity- and roughness-induced crack closure.

The crack tortuosity significantly reduced in the presence of $H_2$. The degree of crack branching decreased, and secondly, when crack branching did occur, the branched crack ceased after a mere short crack growth. Examples of these features in the material are indicated with blue arrows in Figure 9b, which presents the crack path of a 150 barg $H_2$ tested sample. The presence of hydrogen decreased the plastic zone wake at the crack tip by the HELP mechanism, which in turn caused the continuous sharpening of the crack tip during each cycle. The fact that $H_2$ causes the plastic zone at the crack tip to be decreased also explains that the extent of growth of the branches was significantly reduced.

Figure 9c,d are EBSD images showing the crack path in 150 barg $N_2$ and 150 barg $H_2$ weld metal specimens, respectively. From Figure 9c, it is evident that the fracture path in $N_2$ is predominantly transgranular. In contrast, as shown in Figure 9d, decohesion in $H_2$ was primarily intergranular with few transgranular crack path features. The occurrences of transgranular features in $H_2$ are a consequence of the orientation of the microstructure. When the crack passes perpendicular to the acicular ferrite grains, transgranular growth is preferred. In other instances, the crack orientation can be accommodated by crack deflection, enabling an intergranular path to be followed. The fact that intergranular crack growth is observed for the $H_2$ tested specimens emphasizes that the deleterious role of hydrogen fatigue manifests in the grain boundaries. The intergranular fracture characteristics can be related to the HEDE mechanism, which proposes that hydrogen atoms adsorbed to a crack tip or segregated at grain boundaries weaken interatomic bonds and cause atomic decohesion. It can therefore be stated that the fine grains of the weld inherently increase the susceptibility to HA-FCG due to the hydrogen trapping in the grain boundaries. This is in line with the research of Masoumi et al. [47].

### *4.4. Weld Defects*

#### 4.4.1. Macropore Classification

This section identifies the dimensions and locations of defects in the WM based on postmortem analysis of the fracture surface. The effects of these defects on hydrogen fatigue are discussed in the next section (Section 4.4.2). The 150 barg $H_2$ WM samples containing a macropore on the surface were considered defective as they induced a detrimental effect on fatigue life. The pores in this work are classified to be macropores when their length and/or width exceed(s) 500 µm. On average, the macropores had a length and width of ≈800 µm.

In Figure 10a, an overview is provided of a 150 barg $H_2$ WM fracture surface that contained a micro- and macropore. The macropore is shaped as a spheroid with a width and length of ≈500 µm. The micropore is significantly smaller, with a diameter of ≈50 µm. The other 150 barg $H_2$ WM specimen contained a defect that is also shaped as a spheroid and measures a width of ≈1000 µm and a length of ≈1200 µm. This can be seen in Figure 10b. In this figure, the ratchet marks near the tip of the defect are clearly visible. In addition, large cracking is involved, which can be seen from the surface separation. These features highlight the detrimental effects that are associated with the local stress concentration induced by a macro-defect.

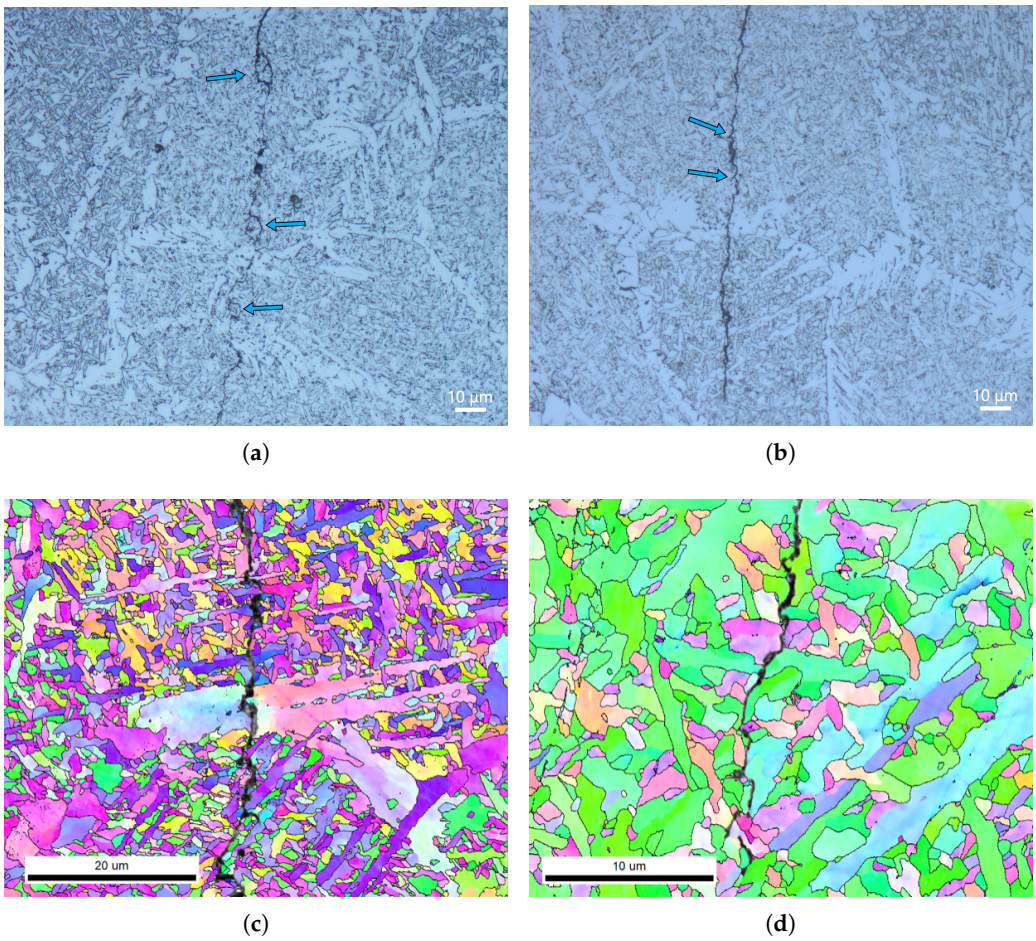


**Figure 9.** Crack path analysis of notched weld metal specimens. (**a**) Optical image of the crack trajectory of a 150 barg $N_2$ tested sample showing metal crumbs (blue arrows). (**b**) Optical image of the virtually straight crack path in a 150 barg $H_2$ tested sample with a minor extent of secondary cracking (blue arrows). (**c**) EBSD image of the predominant transgranular crack trajectory in a 150 barg $N_2$ tested sample. (**d**) EBSD image of the crack trajectory in a 150 barg $H_2$ tested sample showing the predominantly intergranular crack path.

Most WM specimens contained micropores within the range of 10–100 µm regarding the diameter. Figure 10c presents a 150 barg $H_2$ WM fracture surface from which the appearance and distribution of such small micropores can be derived. In both environments ($N_2$ and $H_2$), these micropores did not accelerate the fatigue failure. Therefore, it could be stated that minor weld defects such as these can be neglected in fatigue life time analysis.

#### 4.4.2. Hydrogen-Accelerated Fatigue of Weld Defected Specimens

Figure 11 shows the results of the macroporous defected WM specimens tested under 150 barg $H_2$, along with a comparison of the non-defected 150 barg $N_2$ and $H_2$ WM specimen results. The data used to plot this graph are summarized in Table 5. In Figure 11, the detrimental combinatory effect of macroporous defects and hydrogen can be derived. Relative to the 150 barg $H_2$ non-defected WM specimens, the average number of cycles until failure reduces with a factor of 3.7 when the samples contain macropores. For the defected samples, the average number of cycles until failure is a factor of 11.6 smaller compared to the 150 barg $N_2$ non-defected tested specimens. Hence, this highlights that the worst case scenario for hydrogen fatigue is for macro-porosity in welds.

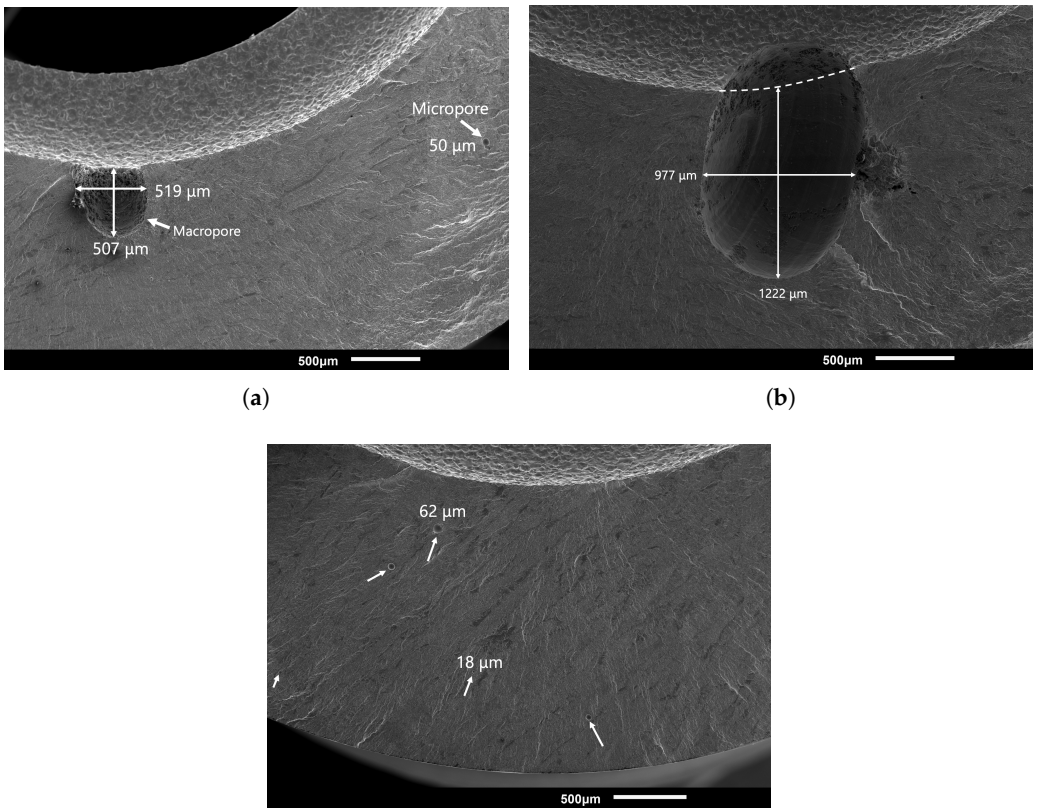


(**a**) (**b**)

(**c**)

**Figure 10.** Macro- and micropore identification of weld metal specimens. (**a**) An overview of a macropore located at the notch. (**b**) Zoomed-in projection of another 150 barg $H_2$ defected weld metal specimen with a macropore located on the notch root. (**c**) Micropores in a 150 barg $N_2$ weld metal specimen. The micropores had a diameter between 10–100 µm.

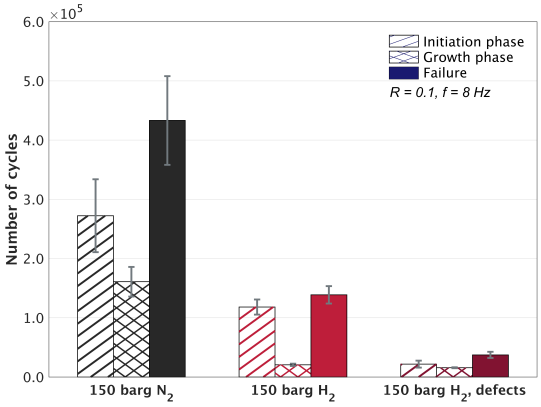


**Figure 11.** Bar graph of the number of cycles spent in the crack initiation phase ($N_I$) and the growth phase ($N_G$), and the total number of cycles until failure ($N_F$) of the weld metal specimens including defected ones. The different conditions tested are shown with distinct colors. The single and double hatched bars represent the number of cycles spent in the initiation and growth phase, respectively. Error bars are standard deviations.

**Table 5.** An overview of the 150 barg tested weld metal fatigue results including defected specimens, presenting the number of cycles spent in the crack initiation phase ($N_I$), the growth phase ($N_G$), the cycles until failure ($N_F$) and percentage of lifetime spent in the crack initiation phase ($L_I$). Errors are standard deviation.

| Material | Environment | $N_I$ [$\times 10^3$] | $N_G$ [$\times 10^3$] | $N_F$ [$\times 10^3$] | $L_I$ [%] |
|---|---|---|---|---|---|
| Weld metal non-defected | 150 barg $N_2$ | 272.3 ± 61.5 | 160.8 ± 25.1 | 433.1 ± 75.0 | 61.3 ± 4.8 |
| | 150 barg $H_2$ | 118.2 ± 12.8 | 20.6 ± 2.0 | 138.8 ± 14.7 | 85.1 ± 0.3 |
| Weld metal defected | 150 barg $H_2$ | 21.7 ± 5.9 | 15.5 ± 0.8 | 37.2 ± 5.2 | 57.1 ± 8.0 |

The $L_I$ of 150 barg $N_2$ non-defected WM specimens and 150 barg $H_2$ defected WM specimens are within the same range. This does not imply that both subsets behave identically. A comparison of $N_G$ for all hydrogen environments (including BM) leads to the conclusion that the number of cycles in the growth phase is relatively constant. To give an indication, $N_G$ in the presence of hydrogen averages 20.3 $\times$ $10^3$ cycles. Taking into account that the lifetime of the porous sample is considerably shorter and that $N_G$ remains the same, one arrives at the result that the relative proportion of $N_G$ increases, which is accompanied by a decrease in $L_I$. This explains the low average of $L_I$ (57.1%) for the 150 barg $H_2$ defected WM specimens. The adverse effect of hydrogen on the lifetime of macroporous specimens manifests in affecting the resistance to crack initiation, which was reduced by 92%. It has been documented that the presence of a local stress raiser may increase HE susceptibility, as a high stress/strain concentration may promote local diffusible hydrogen accumulation [48,49]. A weld defect can therefore readily reach the critical hydrogen concentration required for hydrogen cracking. Thus, the fatigue behavior of the defected WM specimens in hydrogen can be described as follows; the resistance to crack initiation decreases with macropores, but does not additionally accelerate the effect of HA-FCG.

It is recommended that a component should be critically assessed for defects if its intended purpose is related to the exposure of hydrogen environments. However, whether such defects are detected in practice depends to a large extent on the calibration of the non-destructive measurement technique. For instance, considering automatic ultrasonic testing, the detection is dependent on the orientation of the defect (i.e., the length and width) with respect to the measuring direction. According to a report for Shaw Pipelines Services, defects with length $>$ 4 mm down to 1.0 mm in height can be reliably (defined by a 90% probability of detection (POD) value at 95% confidence level) detected by Shaw phased array automated ultrasonic testing [50]. In the worst case, i.e., the scanning direction with a detection limit of 4 mm, the defects mentioned here would not be detected. These findings indicate that such an (undetected) defect may unexpectedly accelerate the failure of hydrogen transporting pipelines.

## 5. Conclusions

This work focused on investigating the effect of hydrogen on fatigue crack initiation and growth in X60 steel and its girth weld. An in situ gaseous hydrogen charging fatigue set-up was used, which internally pressurized specimens with an internal circumferential notch (in the weld). Fatigue crack initiation and growth were successfully measured using a direct current potential drop (DCPD) set-up, which probes the outer surface of the specimen. Several conclusions can be drawn from the experiments with this set-up.

1. This study showed no significant influence of hydrogen on the fatigue crack initiation in the base metal, which was explained by the elastic stress conditions of the fatigue cycles. Nevertheless, the presence of hydrogen reduced the total lifetime by 37%, which was due to hydrogen-accelerated fatigue crack growth (HA-FCG); hydrogen accelerated the crack growth by a factor of 4.

2. For the weld metal, the presence of hydrogen reduced the resistance to crack initiation by 57%, as well as induced HA-FCG (accelerated growth by a factor of 8). The total reduction in fatigue life due to hydrogen was 68% for the weld. The effect of hydrogen on the reduction in lifetime was 1.8 times as high for the weld compared to the base metal. Thus, the deleterious effect of hydrogen on fatigue is more pronounced in the weld metal.
3. The worst case scenario of hydrogen fatigue is for weld defects; at 150 barg hydrogen, the crack growth rate increased by a factor of 11.6 for the specimens including macropores (>500 µm in size). The macropores were identified as spheroids and located on the notch root surface. The macropores reduced the resistance to crack initiation by 92% compared to the non-defected weld metal specimen in 150 barg nitrogen. The detrimental effect of weld defects should therefore not be overlooked in design and repurposing of gas pipelines.
4. No difference on the fatigue behavior was observed between the gas pressures of 70 barg and 150 barg hydrogen. It is postulated that the maximum hydrogen saturation in the crack process zone was already reached at 70 barg.
5. The fracture path of the base metal in nitrogen was transgranular and ductile in nature. In hydrogen, similar fracture behavior was observed prior to HA-FCG. However, after the onset of HA-FCG, the fracture surface transitioned to a mixed-mode transgranular and intergranular quasi-cleavage fracture. The estimated $\Delta K$ for this onset is $>15$ MPa$\sqrt{\text{m}}$. This onset $\Delta K$ related behavior is, however, not observed for the weld metal. From the onset of crack initiation, the weld metal fractures predominantly through an intergranular crack path.
6. The dominant embrittlement mechanisms were HEDE and HELP. The intergranular fracture features were related to the HEDE mechanism. The increased crack tip sharpening and reduced crack tortuosity were attributed to the HELP mechanism.

## 6. Recommendations

It is shown that a variation between 70 and 150 barg of $H_2$ pressure did not affect the crack initiation and overall fatigue life of the weld metal. It is recommended to investigate the effect of different hydrogen pressures further, accompanied by a critical analysis of hydrogen trapping site occupancy. Through such an approach, the effect of hydrogen pressure can be better understood and related to the hydrogen embrittlement mechanisms at play.

In addition, in this research pure hydrogen gas was used to investigate the effect of hydrogen on fatigue behavior. There is a general tendency in literature that oxygen impurities can inhibit hydrogen fatigue. However, those studies that used gas mixtures did not consider weld defects. Performing fatigue tests with different gas blends and/or inhibitors could establish whether crack initiation and growth of weld defected specimens in such cases are affected. This could reveal whether the gas blend or inhibitor can counteract the normally adverse effects of weld defects on hydrogen fatigue, thereby enhancing the safety of hydrogen transport.

This study clearly emphasizes that macropores severely deteriorate fatigue life. It could therefore be inferred that these weld defects are the most deleterious component with regard to hydrogen fatigue. However, other defects can exist in on- and offshore pipes. For example, high-low misalignments in pipeline welds and weld breaks may be present, which can cause cracks in the fusion line or heat-affected zone (HAZ). It remains to be investigated what defect would be most detrimental in a hydrogen environment.

The state-of-the-art would benefit from additional research on hydrogen-accelerated fatigue due to weld porosity defects. Investigating the different effect of weld pores in $N_2$ and $H_2$ environments would add to the understanding of the role weld defects play in $H_2$ environments. Furthermore, additional data are needed regarding the effect of their size and location on hydrogen fatigue. For example, buried macropores were not examined in this work, but this could yield interesting results. An assessment of whether those defects

would be identified by non-destructive testing techniques (i.e., ultrasonic testing) should be included. The feasibility of repurposing hydrogen pipelines would be more reliably assessed through such an approach.

**Author Contributions:** Conceptualization, L.E.F., T.B., T.R., S.P.S. and V.P.; investigation, L.E.F.; supervision, V.P., T.B. and P.L.; writing—original draft preparation, L.E.F.; review and editing, T.B., T.R., S.P.S., P.L. and V.P. All authors have read and agreed to the published version of the manuscript.

**Funding:** This research received no external funding.

**Data Availability Statement:** Data can be made available upon request.

**Conflicts of Interest:** The authors declare no conflict of interest.

## References

1. Ball, M.; Wietschel, M. The future of hydrogen–opportunities and challenges. *Int. J. Hydrog. Energy* **2009**, *34*, 615–627. [CrossRef]
2. European Union Agency for the Cooperation of Energy Regulators (ACER). *Transporting Pure Hydrogen by Repurposing Existing Gas Infrastructure: Overview of Existing Studies and Reflections on the Conditions for Repurposing*; European Union Agency for the Cooperation of Energy Regulators (ACER): Ljubljana, Slovenia, 2021.
3. Nanninga, N.; Slifka, A.; Levy, Y.; White, C. A review of fatigue crack growth for pipeline steels exposed to hydrogen. *J. Res. Natl. Inst. Stand. Technol.* **2010**, *115*, 437–452. [CrossRef] [PubMed]
4. Cialone, H.J.; Holbrook, J.H. Effects of gaseous hydrogen on fatigue crack growth in pipeline steel. *Metall. Mater. Trans. A Phys. Metall. Mater. Sci.* **1985**, *16*, 115–122. [CrossRef]
5. Ronevich, J.A.; Somerday, B.P.; Feng, Z. Hydrogen accelerated fatigue crack growth of friction stir welded X52 steel pipe. *Int. J. Hydrog. Energy* **2017**, *42*, 4259–4268. [CrossRef]
6. Yamabe, J.; Yoshikawa, M.; Matsunaga, H.; Matsuoka, S. Effects of hydrogen pressure, test frequency and test temperature on fatigue crack growth properties of low-carbon steel in gaseous hydrogen. *Procedia Struct. Integr.* **2016**, *2*, 525–532. [CrossRef]
7. Somerday, B.P.; Sofronis, P.; Nibur, K.A.; San Marchi, C.; Kirchheim, R. Elucidating the variables affecting accelerated fatigue crack growth of steels in hydrogen gas with low oxygen concentrations. *Acta Mater.* **2013**, *61.16*, 6153–6170. [CrossRef]
8. Drexler, E.S.; Slifka, A.J.; Amaro, R.L.; Barbosa, N.; Lauria, D.S.; Hayden, L.E.; Stalheim, D.G. Fatigue crack growth rates of API X70 pipeline steel in a pressurized hydrogen gas environment. *Fatigue Fract. Eng. Mater. Struct.* **2014**, *37*, 517–525. [CrossRef]
9. Suresh, S.; Ritchie, R.O. Mechanistic dissimilarities between environmentally influenced fatigue-crack propagation at near-threshold and higher growth rates in lower strength steels. *Met. Sci. J.* **1982**, *16*, 529–538.
10. Shinko, T.; Hénaff, G.; Halm, D.; Benoit, G.; Bilotta, G.; Arzaghi, M. Hydrogen-affected fatigue crack propagation at various loading frequencies and gaseous hydrogen pressures in commercially pure iron. *Int. J. Fatigue* **2019**, *121*, 197–207. [CrossRef]
11. Nguyen, T.T.; Heo, H.M.; Park, J.; Nahm, S.H.; Beak, U.B. Fracture properties and fatigue life assessment of API X70 pipeline steel under the effect of an environment containing hydrogen. *J. Mech. Sci. Technol.* **2021**, *35*, 1445–1455. [CrossRef]
12. Amaro, R.L.; White, R.M.; Looney, C.P.; Drexler, E.S.; Slifka, A.J. Development of a model for hydrogen-assisted fatigue crack growth of pipeline steel. *J. Press. Vessel Technol.* **2018**, *140*, 021403. [CrossRef]
13. Murakami, Y.; Matsuoka, S. Effect of hydrogen on fatigue crack growth of metals. *Eng. Fract. Mech.* **2010**, *77.11*, 1926–1940. [CrossRef]
14. Murakami, Y.; Kanezaki, T.; Mine, Y.; Matsuoka, S. Hydrogen embrittlement mechanism in fatigue of austenitic stainless steels. *Metall. Mater. Trans. A Phys. Metall. Mater. Sci.* **2008**, *39*, 1327–1339. [CrossRef]
15. Matsunaga, H.; Noda, H. Visualization of hydrogen diffusion in a hydrogen-enhanced fatigue crack growth in type 304 stainless steel. *Metall. Mater. Trans. A Phys. Metall. Mater. Sci.* **2011**, *42*, 2696–2705. [CrossRef]
16. An, T.; Zhang, S.; Feng, M.; Luo, B.; Zheng, S.; Chen, L.; Zhang, L. Synergistic action of hydrogen gas and weld defects on fracture toughness of X80 pipeline steel. *Int. J. Fatigue* **2019**, *120*, 23–32. [CrossRef]
17. Chandra, K.; Kain, V.; Kumar, N. Failure Cases of Stainless Steel 316/316L Pipe Welds in Moist Hydrogen Sulfide Environment. *J. Fail. Anal. Prev.* **2022** *22*, 478–490. [CrossRef]
18. An, T.; Peng, H.; Bai, P.; Zheng, S.; Wen, X.; Zhang, L. Influence of hydrogen pressure on fatigue properties of X80 pipeline steel. *Int. J. Hydrog. Energy.* **2017**, *42*, 15669–15678. [CrossRef]
19. An, T.; Zheng, S.; Peng, H.; Wen, X.; Chen, L.; Zhang, L. Synergistic action of hydrogen and stress concentration on the fatigue properties of X80 pipeline steel. *Mater. Sci. Eng. A.* **2017**, *700*, 321–330. [CrossRef]
20. Chen, X.; Ma, L.; Xie, H.; Zhao, F.; Ye, Y.; Zhang, L. Effects of external hydrogen on hydrogen-assisted crack initiation in type 304 stainless steel. *Anti-Corros. Methods Mater.* **2020**, *67*, 331–335. [CrossRef]
21. Bellahcene, T.; Capelle, J.; Aberkane, M.; Azari, Z. Effect of hydrogen on mechanical properties of pipeline API 5L X70 steel. *Appl. Mech. Mater.* **2012**, *146*, 213–225. [CrossRef]
22. Capelle, J.; Gilgert, J.; Pluvinage, G. *Hydrogen Effect on Fatigue and Fracture of Pipe Steels*; Ecole Nationale d'Ingénieurs de Metz: Metz, France, 2009.

23. Hirth, J.P. Effects of hydrogen on the properties of iron and steel. *Metall. Mater. Trans. A Phys. Metall. Mater. Sci.* **1980**, *11*, 861–890. [CrossRef]
24. Turnbull, A. Hydrogen diffusion and trapping in metals. In *Gaseous Hydrogen Embrittlement of Materials in Energy Technologies*; Woodhead Publishing: Teddington, UK, 2012; pp. 89–128.
25. Zhao, Y.; Seok, M.Y.; Choi, I.C.; Lee, Y.H.; Park, S.J.; Ramamurty, U.; Suh, J.Y.; Jang, J.I. The role of hydrogen in hardening/softening steel: Influence of the charging process. *Scr. Mater.* **2015**, *107*, 46–49. [CrossRef]
26. Cialone, H.J.; Holbrook, J.H. Sensitivity of steels to degradation in gaseous hydrogen. In *Hydrogen Embrittlement: Prevention and Control, ASTM STP 962*; Raymond, L., Ed.; American Society for Testing and Materials: Pennsylvania, PA, USA, 1988; pp. 134–152.
27. San Marchi, C.; Somerday, B.P.; Nibur, K.A.; Stalheim, D.G.; Boggess, T.; Jansto, S. Fracture and fatigue of commercial grade API pipeline steels in gaseous hydrogen. In *Pressure Vessels and Piping Conference*; American Society of Mechanical Engineers: Bellevue, WA, USA, 2010; Volume 49255, pp. 939–948.
28. Briottet, L.; Moro, I.; Lemoine, P. Quantifying the hydrogen embrittlement of pipeline steels for safety considerations. *Int. J. Hydrog. Energy* **2012**, *37*, 17616–17623. [CrossRef]
29. Amaro, R.L.; Drexler, E.S.; Rustagi, N.; Nanninga, N.E.; Levy, Y.S.; Slifka, A.J. Fatigue crack growth of pipeline steels in gaseous hydrogen-predictive model calibrated to API-5L X52. In Proceedings of the International Hydrogen Conference (IHC 2012): Hydrogen-Materials Interactions, Moran, Wyoming, 9–12 September 2012; Sofronis, P., Somerday, B.P., Eds.; ASME Press: Jackson Lake, WY, USA, 2012; pp. 329–338.
30. Slifka, A.J.; Drexler, E.S.; Stalheim, D.G.; Amaro, R.L.; Lauria, D.S.; Stevenson, A.E.; Hayden, L.E. The Effect of Microstructure on the Hydrogen-Assisted Fatigue of Pipeline Steels. In *Proceedings of the ASME 2013 Pressure Vessels and Piping Conference*, American Society of Mechanical Engineers, Paris, France, 14–18 July 2013; Volume 55713, p. V06BT06A009.
31. Ronevich, J.A.; Somerday, B.P.; San Marchi, C.W. Effects of microstructure banding on hydrogen assisted fatigue crack growth in X65 pipeline steels. *Int. J. Fatigue*, **2016**, *82*, 497–504. [CrossRef]
32. Boot, T.; Riemslag, T.; Reinton, E.; Liu, P.; Walters, C.L.; Popovich, V. In-Situ Hollow Sample Setup Design for Mechanical Characterisation of Gaseous Hydrogen Embrittlement of Pipeline Steels and Welds. *Metals*, **2021**, *11*, 1242. [CrossRef]
33. Arnaudov, N. Micromechanical simulation of fatigue crack initiation under hydrogen influence. In *Stuttgart: Materialprüfungsanstalt (MPA)*; Universität Stuttgart: Stuttgart, Germany, 2021; pp. 47–53; ISBN 9783946789109.
34. Mughrabi, H. On the life-controlling microstructural fatigue mechanisms in ductile metals and alloys in the gigacycle regime. *Fatigue Fract. Eng. Mater. Struct.* **1999**, *22*, 633–641. [CrossRef]
35. Zhang, Z.; Obasi, G.; Morana, R.; Preuss, M. Hydrogen assisted crack initiation and propagation in a nickel-based superalloy. *Acta Mater.* **2016**, *113*, 272–283. [CrossRef]
36. Uyama, H.; Nakashima, M.; Morishige, K.; Mine, Y.; Murakami, Y. Effects of hydrogen charge on microscopic fatigue behaviour of annealed carbon steels. *Fatigue Fract. Eng. Mater. Struct.* **2006**, *29*, 1066–1074. [CrossRef]
37. Holbrook, J.H.; Cialone, H.J.; Mayfield, M.E.; Scott, P.M. *Effect of Hydrogen on Low-Cycle-Fatigue Life and Subcritical Crack Growth in Pipeline Steels*; Battelle Columbus Labs: Columbus, OH, USA, 1982.
38. Zhang, S.; Li, J.; An, T.; Zheng, S.; Yang, K.; Lv, L.; Xie, C.; Chen, L.; Zhang, L. Investigating the influence mechanism of hydrogen partial pressure on fracture toughness and fatigue life by in-situ hydrogen permeation. *Int. J. Hydrog. Energy.* **2021**, *46*, 20621–20629. [CrossRef]
39. Amaro, R.L.; Drexler, E.S.; Slifka, A.J. Fatigue crack growth modeling of pipeline steels in high pressure gaseous hydrogen. *Int. J. Fatigue* **2014**, *62*, 249–257. [CrossRef]
40. Sachs, N.W. Understanding the surface features of fatigue fractures: How they describe the failure cause and the failure history. *J. Fail. Anal. Prev.* **2005**, *5*, 11–15. [CrossRef]
41. Ogawa, Y.; Umakoshi, K.; Nakamura, M.; Takakuwa, O.; Matsunaga, H. Hydrogen-assisted, intergranular, fatigue crack-growth in ferritic iron: Influences of hydrogen-gas pressure and temperature variation. *Int. J. Fatigue* **2020**, *140*, 105806. [CrossRef]
42. Slifka, A.J.; Drexler, E.S.; Nanninga, N.E.; Levy, Y.S.; McColskey, J.D.; Amaro, R.L.; Stevenson, A.E. Fatigue crack growth of two pipeline steels in a pressurized hydrogen environment. *Corros. Sci.* **2014**, *78*, 313–321. [CrossRef]
43. Marsh, P.G.; Gerberich, W.W. Influence of microstructure and texture on fatigue crack initiation in HSLA steel in hydrogen and nitrogen atmospheres. In Proceedings of the First International Conference on Microstructures and Mechanical Properties of Aging Materials, Chicago, IL, USA, 2–5 November 1992; pp. 282–292.
44. Igwemezie, V.; Mehmanparast, A.; Brennan, F. The influence of microstructure on the fatigue crack growth rate in marine steels in the Paris Region. *Fatigue Fract. Eng. Mater. Struct.* **2020**, *43*, 2416–2440. [CrossRef]
45. Hu, Y.; Wang, B.; Xu, Y.; Wang, L.; Cheng, W. Investigation on the fatigue crack propagation behavior of L360MS pipeline steel welded joints with Inconel 625 weld metal. *Trans. Indian Inst. Met.* **2020**, *73*, 2387–2402. [CrossRef]
46. Bui, T. P.; Miyashita, Y.; Morikage, Y.; Tagawa, T.; Handa, T.; Mutoh, Y.; Otsuka, Y. Contributions of grain size and crystal orientation to fatigue crack deflection and branching behavior in low carbon steel plates. *ISIJ Int.* **2021**, *61*, 424–433. [CrossRef]
47. Masoumi, M.; Santos, L.P.; Bastos, I.N.; Tavares, S.S.; da Silva, M.J.; de Abreu, H.F. Texture and grain boundary study in high strength Fe–18Ni–Co steel related to hydrogen embrittlement. *Mater. Des.* **2016** *91*, 90–97. [CrossRef]
48. Wang, M.; Akiyama, E.; Tsuzaki, K. Effect of hydrogen and stress concentration on the notch tensile strength of AISI 4135 steel. *Mater. Sci. Eng. A Struct. Mater.* **2005**, *398*, 37–46. [CrossRef]

49. Díaz, A.; Alegre, J.M.; Cuesta, I.I. Numerical simulation of hydrogen embrittlement and local triaxiality effects in notched specimens. *Theor. Appl. Fract. Mech.* **2017**, *90*, 294–302. [CrossRef]
50. *Shaw Pipeline Services Phased Array AUT Qualification*; Det Norske Veritas: Houston, TX, USA, 2009.